9-1-2007

Kinematical studies of the low-mass X-ray binary GR Mus (XB 1254-690)

A. D. Barnes
University of Southampton

J. Casares
Instituto Astrofisico de Canarias

R. Cornelisse
University of Southampton

P. A. Charles
University of Southampton

D. Steeghs
Harvard-Smithsonian Center for Astrophysics

See next page for additional authors

Recommended Citation

Barnes, A., Casares, J., Cornelisse, R., Charles, P., Steeghs, D., Hynes, R., & O'Brien, K. (2007). Kinematical studies of the low-mass X-ray binary GR Mus (XB 1254-690). *Monthly Notices of the Royal Astronomical Society, 380* (3), 1182-1190. https://doi.org/10.1111/j.1365-2966.2007.12174.x

Mon. Not. R. Astron. Soc. **380,** 1182–1190 (2007) doi:10.1111/j.1365-2966.2007.12174.x

Kinematical studies of the low-mass X-ray binary GR Mus (XB 1254–690)

A. D. Barnes,[1⋆] J. Casares,[2] R. Cornelisse,[1] P. A. Charles,[1,3] D. Steeghs,[4,5] R. I. Hynes[6] and K. O'Brien[7]

[1]*School of Physics and Astronomy, University of Southampton, Southampton SO17 1BJ*
[2]*Instituto de Astrofisica de Canarias, 38200 La Laguna, Tenerife, Spain*
[3]*South African Astronomical Observatory, PO Box 9, Observatory 7935, Cape, South Africa*
[4]*Harvard-Smithsonian Centre for Astrophysics, MS-67, 60 Garden Street, Cambridge, MA 02138, USA*
[5]*Department of Physics, University of Warwick, Coventry CV4 7AL*
[6]*Department of Physics and Astronomy, 202 Nicholson Hall, Louisiana State University, Baton Rouge, LA 70803, USA*
[7]*European Southern Observatory, Casilla 19001, Santiago 19, Chile*

Accepted 2007 June 28. Received 2007 June 22; in original form 2007 May 31

ABSTRACT

We present simultaneous high-resolution optical spectroscopy and X-ray data of the X-ray binary system GR Mus (XB 1254–690), obtained over a full range of orbital phases. The X-ray observations are used to re-establish the orbital ephemeris for this source. The optical data include the first spectroscopic detection of the donor star in this system through the use of the Doppler Tomography technique on the Bowen fluorescence blend (∼4630–4650 Å). In combination with an estimate for the orbital parameters of the compact object using the wings of the He II λ4686 emission line, dynamical mass constraints of $1.20 \leqslant M_X/\mathrm{M}_\odot \leqslant 2.64$ for the neutron star and $0.45 \leqslant M_2/\mathrm{M}_\odot \leqslant 0.85$ for the companion are derived.

Key words: binaries: close – binaries: spectroscopic – stars: individual: GR Mus – stars: individual: XB 1254–690 – X-rays: binaries.

1 INTRODUCTION

XB 1254–690 is a persistently bright, low-mass X-ray binary (LMXB). It was identified with a faint blue star (GR Mus, $V = 19.1$), which exhibited the Bowen blend of N III and C III in emission (Griffiths et al. 1978). The object produced type 1 X-ray bursts (Mason et al. 1980; Courvoisier et al. 1986), indicating the presence of a neutron star as the compact object. Dips of up to 95 per cent of the 1–10 keV flux, with a recurrence period of $P_X = 3.88 \pm 0.15$ h and lasting ∼0.8 h per cycle, were discovered in *EXOSAT* data by Courvoisier et al. (1986). The dips are caused by obscuration of the central source by a bulge on the outer edge of the accretion disc, implying a moderately high inclination.

From *V*-band observations of the optical counterpart, Motch et al. (1987) determined an optical ephemeris where minimum light occurs at $T_{\min} = \mathrm{JD}\ 244\,5735.693\ (4) + 0.163\,890\ (9)$ d, equivalent to a period of $P_{\mathrm{opt}} = 3.9334 \pm 0.0002$ h. This broad optical modulation is probably due to the changing visibility of the heated face of the secondary star in the system, with an additional contribution from the X-ray heated bulge, although other explanations such as an asymmetrical disc or occultation of the disc by the companion cannot be ruled out. Within the errors, the optical and X-ray period measurements are consistent, with later X-ray observations indicating that the optical modulation provides a more accurate measurement of the orbital period (Smale, Church & Balucinska-Church 2002; Levine & Corbet 2006). A short section of simultaneous X-ray and optical coverage showed that the optical minimum occurs ∼0.16 in phase after the centre of the X-ray dips (Motch et al. 1987).

Simple geometrical modelling is possible by considering the X-ray illuminated area of the companion star, disc radius, disc opening angle and inclination at given distances which are compatible with the observed optical flux and the amplitude of the light curve. This leads to constraints on the source inclination of 65°–73°, and on the distance of 8–15 kpc (Motch et al. 1987).

The first mass constraints for this system were based upon a unique relation between the orbital period and the mass of the companion, assuming that the companion is a low-mass, zero-age main-sequence star filling its Roche lobe (Warner 1976). Using this approximation, Courvoisier et al. (1986) estimate the mass of the companion to be in the region of $\sim 0.45\,\mathrm{M}_\odot$.

The first kinematic mass constraints were proposed by Cowley, Hutchings & Crampton (1988), who obtained intermediate-resolution (∼3 Å) spectra using the 4-m telescope at the Cerro Tololo Inter-American Observatory. Assuming that velocities derived from the He II λ4686 emission line centroid represent the motion of the compact star and not, for example, the streaming of gas between the stars or out of the system, then approximate stellar masses can be derived using the mass function. The result is consistent with a low-mass main-sequence star ($M \simeq 0.5-0.8\,\mathrm{M}_\odot$) and a canonical $1.4\,\mathrm{M}_\odot$ neutron star.

⋆E-mail: adb@astro.soton.ac.uk

Table 1. Log of observations of GR Mus/XB 1254–690.

HJD	Observatory	Total int. time (h)
245 3151.52	VLT	3.75
245 3151.51	*RXTE*	4.75
245 3152.52	VLT	4
245 3152.69	*RXTE*	5.25
245 3153.53	VLT	2

In the remainder of this paper, we will attempt to confirm and better constrain these mass estimates using high-resolution blue optical spectroscopy. We will measure the wings of the He II λ4686 emission line to gain an estimate for the compact object velocity (Section 3.3), and use the Bowen fluorescence technique (Steeghs & Casares 2002) to measure the donor star velocity (Section 3.4). We also obtained simultaneous X-ray observations (see Section 3.1) in order to re-establish the ephemeris of Motch et al. (1987). This cannot be extended to the observations described herein because the propagated uncertainty in phase is now comparable to the orbital period itself.

2 OBSERVATIONS

We have obtained simultaneous optical and X-ray data for GR Mus/XB 1254–690. The journal of observations is given in Table 1.

2.1 Optical data

Phase-resolved spectroscopy of GR Mus was obtained from 2004 May 26 to 28 using the FORS 2 spectrograph mounted on the VLT/UT4 at European Southern Observatory (ESO)'s Paranal observatory. During each night, we observed GR Mus for $\simeq$ one full orbit, resulting in a total of 38 spectra with an integration time of 900 s each. We used the 1400 V volume-phased holographic grism, and a slit width of 0.7 arcsec, giving a wavelength coverage of λλ4513-5814 with a resolution of 70 km s^{-1} (FWHM). The seeing during these observations varied between 0.5 and 2.1 arcsec. The slit was orientated at a position angle of 88.°15 to include a comparison star in order to calibrate slit losses. We observed the flux standard Feige 110 with the same instrumental setup in order to correct for the instrumental response. He, Ne, Hg and Cd arc lamp exposures were taken during daytime for the wavelength calibration scale. We de-biased and flat-fielded all of the images and used optimal extraction techniques to maximize the signal-to-noise ratio of the extracted spectra (Horne 1986). The pixel-to-wavelength scale was derived through polynomial fits to a large number of identified reference lines resulting in a dispersion of 0.64 Å pixel^{-1}. Velocity drifts due to instrumental flexure (found to be always $<$5 km s^{-1}) were corrected by cross-correlation with the sky spectra.

2.2 X-ray data

Simultaneous X-ray data from XB 1254–690 were obtained using the Proportional Counter Array (PCA) onboard the *Rossi X-Ray Timing Explorer* (*RXTE*). The PCA [for a detailed description, see Jahoda et al. (1996)] onboard the *RXTE* satellite consists of an array of five co-aligned Proportional Counter Units (PCUs) that are sensitive to photons of energy 2 to 60 keV with a total collecting area of 6500 cm^2. We obtained 36 ks of total coverage during our optical observations. For our analysis we only used the data from the Standard 2 configuration, with a time resolution of 16 s.

3 ANALYSIS

3.1 Determination of orbital phase

The ephemeris of Motch et al. (1987) is now out of date because the propagated uncertainty in phase is over a factor of 2 greater than the orbital period. We therefore need to make use of our contemporaneous *RXTE* observations to set a new zero-point using the X-ray dips [Note that we still use the Motch et al. (1987) orbital period.] This is not quite as simple as it would first appear since there are large variations in dip depth and structure that are apparent from observation to observation, as well as cycle to cycle (Courvoisier et al. 1986). Additionally, a note of caution must be sounded since in a number of earlier *RXTE* and *BeppoSAX* observations (Smale & Wachter 1999; Iaria et al. 2001), X-ray dipping was not observed at all, with an accompanying decrease in the mean optical variability of the source. With the combination of these effects, it was suggested that the vertical structure on the accretion disc edge, associated with the impact point of the accretion stream, had decreased in angular size at the time of these earlier observations. The cause of this intermittent reduction in opening angle is not understood. Our observations include just one deep dipping episode (Fig. 1), co-incident with our first night of optical observations.

XB 1254–690 typically exhibits 'shoulders' of dipping, i.e. regions both before and after the deep dipping in which there is a small decrease of intensity. Each shoulder of the dip lasts ∼650–925 s, during which the total count rate in the 2–25 keV band drops by ∼15 per cent with no strong changes in the hardness ratio. The shoulder is followed by an interval of strongly variable deep dipping lasting ∼1100 s (Smale et al. 2002), with associated strong changes in the hardness ratio (Fig. 2). The hardening of the spectra in the dips is most likely to be due to absorption by cold matter.

Our observation of a dipping episode opens with the system already in the first shoulder phase, the onset of deep dipping occurring approximately 200–250 s into the observation (before a brief return of the source intensity to the non-dip level), and then continuing to capture the full egress from deep dipping, into the shoulder and then

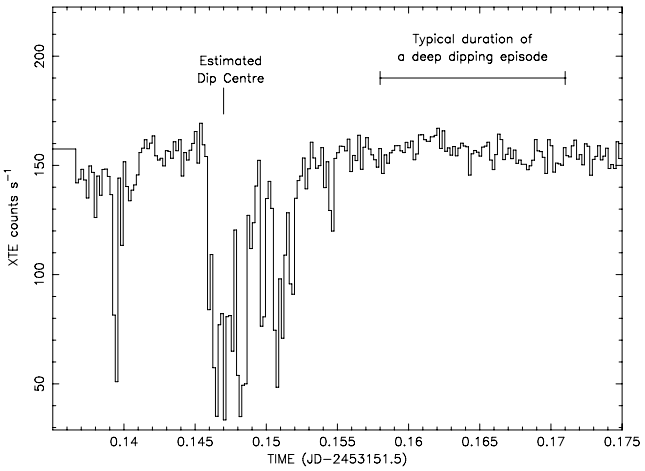

Figure 1. 2–20 keV X-ray light curve showing the deep dip used to calibrate a new ephemeris for the system. The dipping episode appears to begin shortly before JD 245 3151.64, and occurs for the typical dip duration of ∼1100 s (Smale et al. 2002).

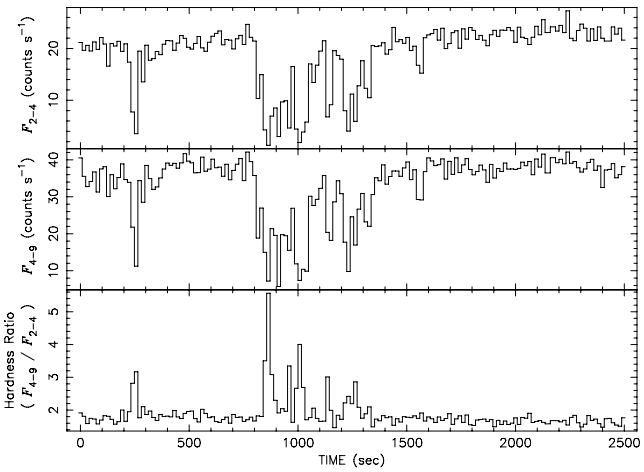

Figure 2. 2–4 keV (top) and 4–9 keV (centre) X-ray light curves displaying the deep dipping episode. The bottom panel displays hardness as a function of intensity. There is an anticorrelation between intensity and hardness ratio during the deep dipping episode, which begins shortly after 200 s on the above scale.

returning to the continuum level. Note that the return of the source intensity to the non-dip level during this episode is not unusual, and the light curve can in fact be interpreted as superpositions of small micro-dips (e.g. Uno et al. 1997).

Unfortunately, the lack of information regarding the full ingress to deep dipping through the preceding shoulder introduces a degree of uncertainty into our estimate of the dip centre. For example, we could potentially be observing only a small section of an extended deep dipping episode [Uno et al. (1997) report dips lasting for ∼40 min]. If this is the case, the absence of the beginning of the dip will cause the estimate for dip centre to be incorrect. Nevertheless, we do have cause for optimism. The deep dipping which we observe is approximately 1100 s in length, equivalent to the typical period of a dipping episode in XB 1254–690 (see above). This is a strong indicator that we have full, or nearly full, coverage of the deep dipping phase. We estimate the dip centre by eye, taking the mid-point between the onset of and exit from deep dipping (which can be determined with the help of the associated hardness ratio changes; see Fig. 2). This occurs at $T_{\rm dip} = {\rm JD}\ 245\,3151.647$ (3). From Motch et al. (1987), we know that the dip centre has an average orbital phase of 0.84 (with phase 0 occurring at optical minimum). We therefore estimate a new value for T_0 of JD 245 3151.509 (3).

There are problems with the reliability of an ephemeris generated from just a single dipping episode, not least because we do not have full coverage on either side of the dip. It is therefore hard to estimate the dip centre with absolute confidence. However, we are encouraged by the fact that our dip lies within 0.05 phase of the 1999 dips (the propagated phase uncertainty from these dips is of the order of ∼0.6) reported by in't Zand et al. (2003). More importantly, the continuum light curve from the resulting ephemeris possesses the same phasing relation reported by Motch et al. (1987) (Fig. 3).[1] In light of this evidence, we are confident that we have identified the dip centre correctly and we will use this zero-point to calculate orbital phases throughout the remainder of this paper.

[1] Note that the large intrinsic scatter in the optical continuum light curve makes the generation of a new ephemeris solely from a relatively limited data set such as ours rather difficult.

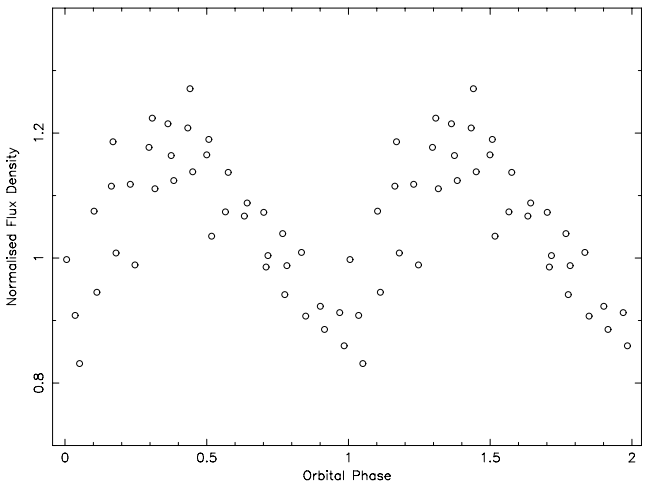

Figure 3. Continuum light curve of GR Mus, normalized to the flux level of the first observation in our data set. Note that the errors on each measurement are smaller than the plotted points.

3.2 Optical emission spectrum

The continuum-subtracted average of the 38 individual optical spectra, corresponding to an exposure time of nearly 10 h, is given in Fig. 4. The overall spectrum resembles that of other LMXBs, with high excitation lines superposed on a blue continuum. This is typical of strongly X-ray heated accretion discs (e.g. van Paradijs & McClintock 1995).

The blue end of the optical spectrum in this system is dominated by the Bowen emission blend of C III and N III. He II λ4686 is also seen strongly in emission, in addition to weaker Hβ and He II λ5411. The absorption component longward of Hβ is observed in a few other LMXBs such as X 1822–371 (Casares et al. 2003), XTE J2123–058 (Hynes et al. 2001), GX 339–4 (Buxton & Vennes 2003) and MM Ser (Hynes et al. 2004).

The narrow emission feature at 5577 Å is [O I], a strong night-sky line useful for confirming the veracity of our wavelength calibration. The broad features between 4900 and 5300 Å remain unidentified. The absence of these features in our comparison star led us to believe that they are real. We also see some of these 'bumps' in other

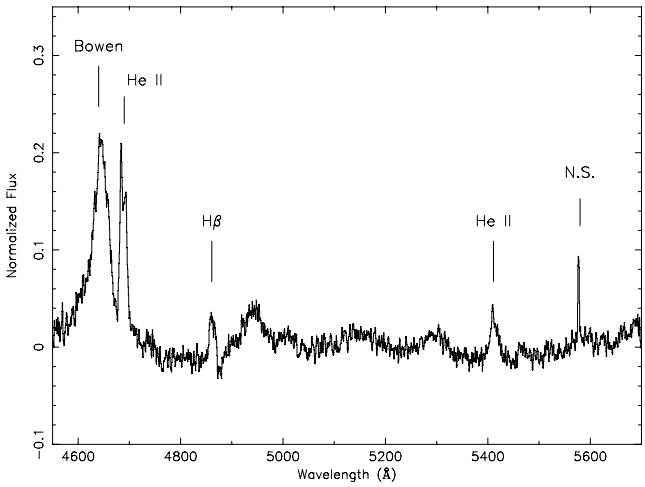

Figure 4. Average normalized spectrum of GR Mus. The most prominent emission lines are indicated, including the Bowen blend of C III and N III, He II and Hβ. The emission line near 5577 Å is a night sky feature.

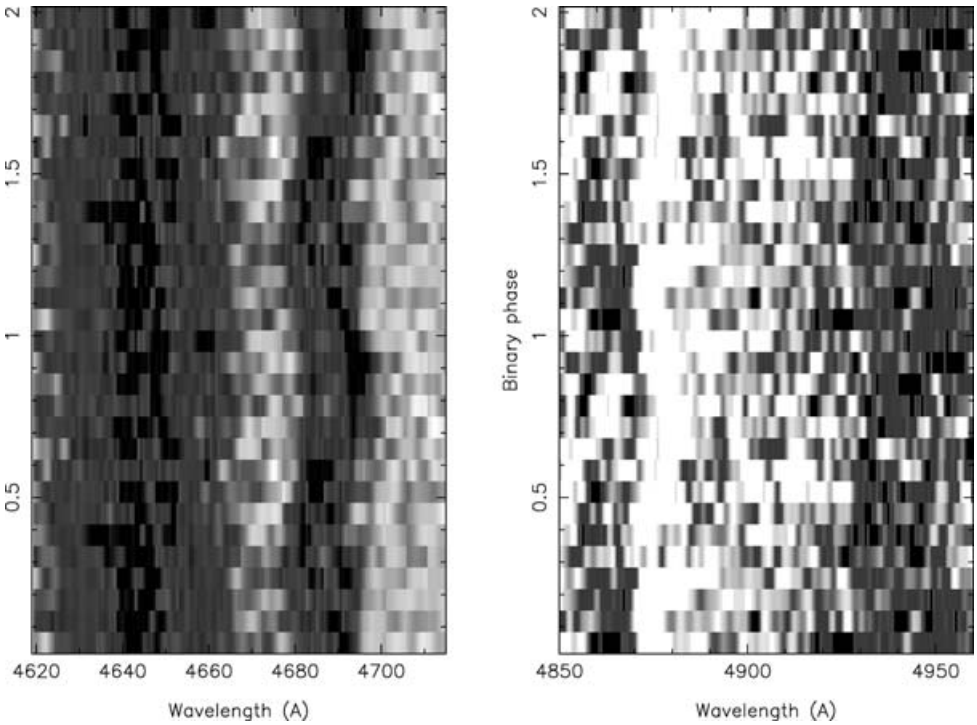

Figure 5. Trailed spectra of the Bowen complex and He II λ4686 (left-hand panel) and the Hβ region (right-hand panel). The data are plotted twice for clarity. Note that the wavelength scales differ. There are clear multiple S-waves evident in the He II emission line, ∼0.25 out of phase with each other, and also in the Bowen complex. The absorption component redwards of Hβ is present at all phases.

LMXBs (e.g. GX 9+9, X 1822–371, V801 Ara, V926 Sco), and perhaps they are blends of a number of different weak emission lines. Part of this could be He I λ4922 and λ5016, and also Fe II λ4924, λ5018, λ5169 and λ5297. There are also several O II and O III lines between 4891 and 5006 Å which may explain the large bump at ∼4930 Å. Note also that the Bowen blend (and to a lesser extent the He II λ4686 emission line) appears to be sitting upon a broad emission 'hump'. This has been noted in other LMXBs (e.g. V801 Ara; Augusteijn et al. 1998), and attributed to a blend of Fe II emission lines (Schachter, Filippenko & Kahn 1989).

In Fig. 5, we display the Bowen blend and He II λ4686 in the form of a trailed spectrogram. All of the individual spectra were first normalized to the continuum using a third-order polynomial fit, and then phase-folded into 15 bins. The spectra were then smoothed using a Gaussian filter with a FWHM of two pixels. We see a clear S-wave structure modulated on the orbital period in the He II λ4686 emission. The blue-to-red crossing phase is ∼0.6 and the semi-amplitude ∼250 km s^{-1}. This behaviour indicates a close association with the accretion disc or compact object. There is also an additional, weaker, component present. Again, this is modulated on the orbital period, approximately a quarter cycle out of phase with the more prominent component. There also appear to be faint traces of two antiphased sharp components in the Bowen blend though the broad underlying component moves in phase with the accretion disc S-wave (maximum blue-shift at phase 0.25). The tomograms discussed in Section 3.4 will help to characterize these spectral trails more thoroughly.

The Hβ line is shown in the right-hand panel in Fig. 5, along with the broad emission feature at ∼4930 Å. The absorption component longward of Hβ is present at all phases, and in common with the emission component displays an S-wave approximately in phase with the expected motion of the accretion disc. The broad feature at ∼4930 Å also displays an S-wave. The He II λ5411 emission line is too weak in the individual spectra to produce a trailed spectrogram.

3.3 Motion of the compact object

Early attempts to determine any kinematic constraints on this system met with limited success. Motch et al. (1987) noted that the relative weakness of the emission lines in their spectra did not allow for the study of their variation with orbital phase. However, they did exclude the possibility of orbital motion of He II λ4686 (which requires a source of highly ionizing radiation, and is typically seen in accretion discs) in excess of 300 km s^{-1}. Later observations by Cowley et al. (1988) did result in a measurement of the same He II line's core velocity, which possessed a semi-amplitude of 114 ± 13 km s^{-1}. However, this is not a particularly reliable measurement of the compact object velocity. The line core can often be heavily contaminated by other emission sites (see Fig. 6), for example, from the accretion stream or 'hot-spots' on the accretion disc itself.

Instead, the compact object velocity can be better estimated by examining the wings of the emission line. These wings find their origin in the high-velocity gas of the inner accretion disc, very close to the compact object itself. Presumably, this gas will closely replicate the motion of the compact object, and it is far less likely that alternative emission sites will provide a strong contaminating effect. However, this method is not immune to contamination and we must be cautious in accepting the results of this analysis.

We have followed the double-Gaussian technique (Schneider & Young 1980) to estimate both the velocity semi-amplitude K_1 and the systemic velocity γ of the compact object from He II λ4686. We employed a double Gaussian bandpass with FWHM of 100 km s^{-1} and Gaussian separations of 300–1700 km s^{-1} in steps of 100 km s^{-1}. Radial velocity curves of line sections with

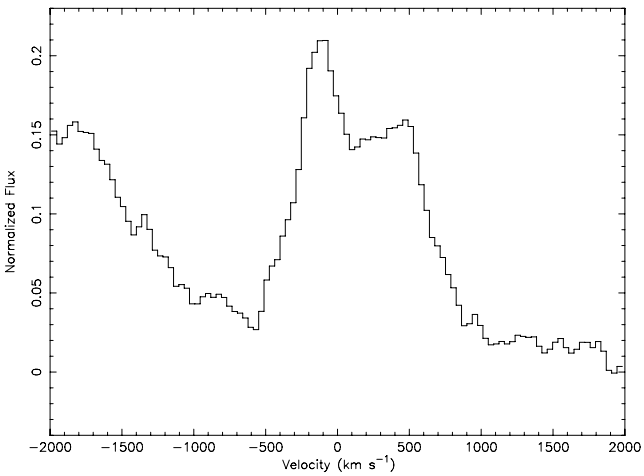

Figure 6. Velocity profile of the He II λ4686 emission line displaying a complex core structure. The extreme blue wing is contaminated by the Bowen emission blend.

separations of 700–1400 km s^{-1} yield consistent results with a median blue-to-red crossing phase of 0.58 ± 0.03, median velocity semi-amplitude $K_1 = 130 \pm 16$ km s^{-1} and median systemic velocity $\gamma = 173 \pm 12$ km s^{-1} (Fig. 7). The errors are conservatively taken from the maximum error obtained from sine wave fits to the results from each individual line section. Separations below 700 km s^{-1} suffer badly from contamination by the line core, whilst separations over 1400 km s^{-1} become corrupted by continuum noise and the Bowen emission blend. The small difference in phasing (0.08 orbits; slightly larger than the ephemeris uncertainty of ∼0.02 orbits) indicates that even the line wings may be contaminated to some extent by inhomogeneities in the disc. This contamination will also affect the measurements of K_1 and γ to some extent. For example, if the accretion disc is warped, then the double-Gaussian technique's assumption of a symmetrical accretion disc will be incorrect and the estimates will be compromised. Nevertheless, this remains the best method for estimating K_1 from our own and other currently available data.

Unfortunately, the He II λ5411 and Hβ emission lines, which are clearly seen in our averaged spectrum (Fig. 4), are too weak in the individual spectra for a similar analysis. The fitting procedures are simply dominated by noise.

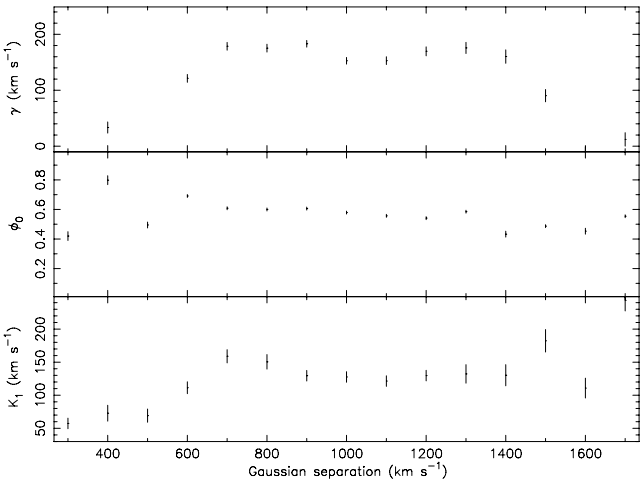

Figure 7. Diagnostic diagram for the He II λ4686 emission line wings displaying the systemic velocity γ (top), phasing (centre) and radial velocity K_1 (bottom).

3.4 Doppler tomography

We can use Doppler tomography (Marsh & Horne 1988) to measure the radial velocity amplitudes of any weak, narrow, emission lines that may be present. By mapping the observed data on to a velocity coordinate frame, Doppler tomography makes use of all data at once and can thus be used to search for features that are too weak to be distinguished in each individual spectrum. One effectively resolves the distribution of line emission in the co-rotating frame of the binary system, providing an excellent tool for identifying the origin and kinematics of the various emission components. It also allows us to map the emission line distribution from the broader He II and Hβ lines.

Secondary star emission is readily identifiable in Doppler tomograms since the solid body rotation of the Roche lobe is mapped to a corresponding Roche lobe area along the positive V_y-axis. For reference, in Figs 8–11 we overplot the area of the Roche lobe and the centres of mass of the donor star (uppermost cross), full system (map centre) and the compact object (lower cross) assuming a mass ratio of ∼0.4 (equivalent to the mass ratio proposed by Cowley et al. 1988) and compact object velocity of 130 km s^{-1}. Additionally, we have overplotted the ballistic accretion stream for such a system. The circle, centred upon the compact object and with radius 600 km s^{-1}, indicates the common emission regions from a generic LMXB accretion disc. We employed a maximum entropy implementation of Doppler tomography whereby the data are fitted under the added constraint of maximizing the entropy (i.e. image

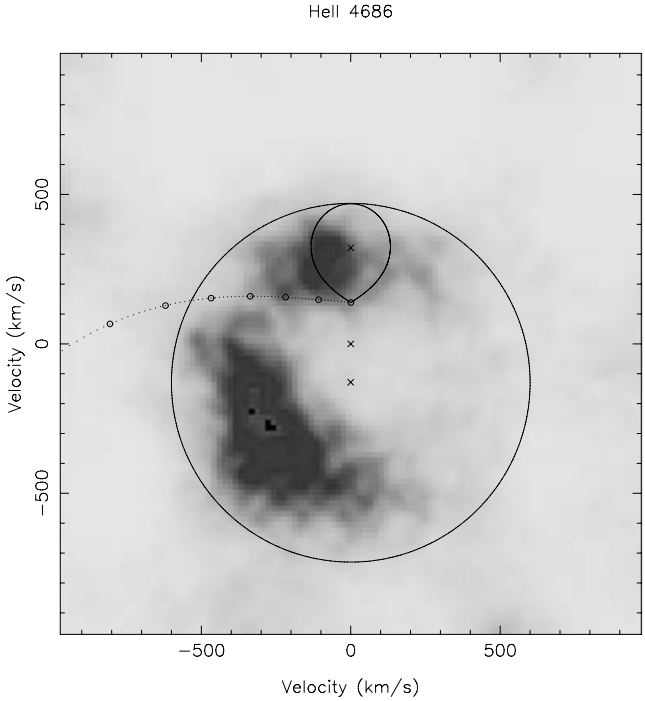

Figure 8. Doppler tomogram reconstructed from the He II λ4686 emission line using maximum entropy optimisation, $\gamma = 185$ km s^{-1}. The area of the Roche lobe, the ballistic accretion stream and the centres of mass of the donor star (uppermost cross), system (map centre) and the compact object (lower cross) are plotted assuming a mass ratio of ∼0.4 and compact object velocity of 130 km s^{-1}. The circle is centred upon the compact object and possesses a radius of 600 km s^{-1}.

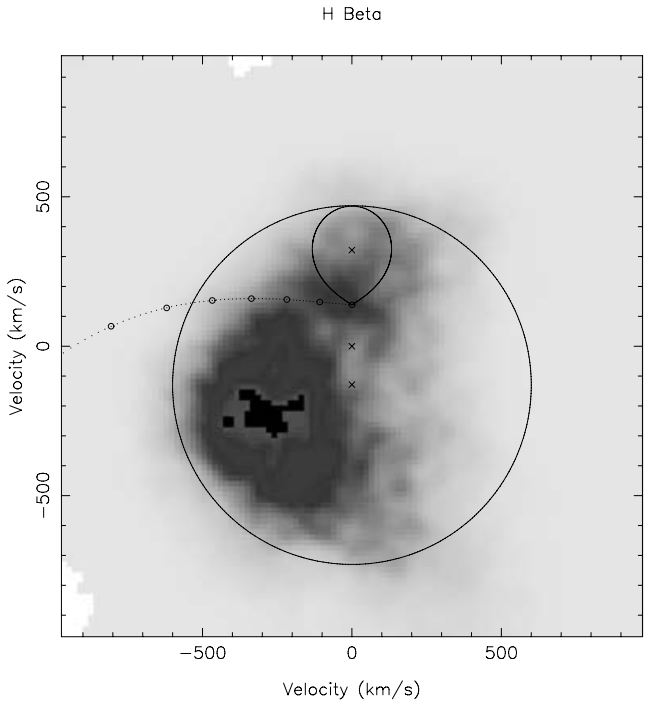

Figure 9. Doppler tomogram reconstructed from the Hβ emission line using maximum entropy optimisation, $\gamma = 185$ km s^{-1}. The symbols are as for Fig. 8.

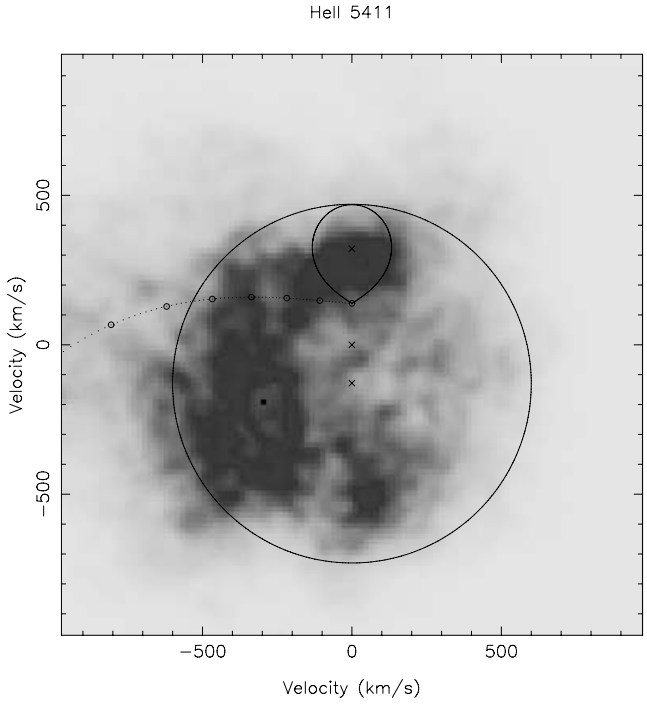

Figure 10. Doppler tomogram reconstructed from the He II λ5411 emission line using maximum entropy optimization, $\gamma = 185$ km s^{-1}. The symbols are as for Fig. 8.

smoothness) of the tomogram (Marsh & Horne 1988). This reduces the presence of noise artefacts in the recovered tomograms and allows for a simultaneous fit to a number of heavily blended lines.

In Fig. 8, we display a tomogram of the He II λ4686 emission line. This displays a clear enhancement in the lower left quadrant

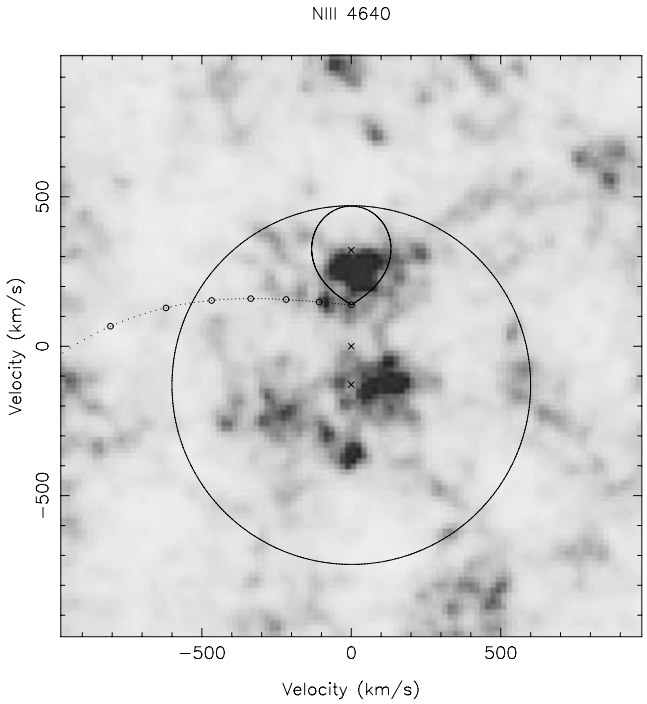

Figure 11. Doppler tomogram reconstructed from the N III λ4640 emission line using maximum entropy optimization, $\gamma = 185$ km s^{-1}. The symbols are as for Fig. 8.

and an additional component close to the accretion stream. We do not observe the classic ring-like distribution of the accretion disc, presumably due to the strength of the line core features vastly overwhelming the high-velocity inner disc emission. For this reason, we cannot be fully confident in the results of the double Gaussian technique (see Section 3.3), though this remains at present the best method for estimating K_1.

The enhancement in the (lower) left quadrant is also seen in the tomograms of Hβ (Fig. 9) and He II λ5411 (Fig. 10). Whilst this phenomenon is a common feature in the remarkable SW Sex type systems (Hellier 2000), it has also been noted in some other LMXBs, notably XTE J2123–058 (Hynes et al. 2001), GX 9+9 (Cornelisse et al. 2007) and J 0422+32 (Casares et al. 1995). However, in this case (and in the case of X 1636–536 and X 1735–444; Casares et al. 2007) the emission is not quite so localized in the lower-left quadrant, but is present in a broad-band on the left-hand side of the maps. Rather than being an analogue to the highly magnetic SW Sex type systems, it is likely that this emission is produced in an extended disc bulge. In most LMXBs, the He II emission is predominantly produced in a hotspot where the accretion stream impacts the disc (thus producing a spot in the upper left quadrant of a Doppler map; e.g. Pearson et al. 2006) or is more evenly distributed around the bulk of the accretion disc. If the emitting gas was symmetrically distributed around the primary, the Doppler image would reveal a circular distribution centred on $V_x = 0, V_y = -K_1$. This would have been a useful way of confirming the K_1 estimate derived from the wings of the He II λ4686 emission line.

Like He II λ4686, the He II λ5411 tomogram also indicates the presence of some diffuse emission at velocities which partially correspond to the Roche lobe of the donor star. However, as this emission is diffuse in the Doppler map, extending over a broad range of velocities, it is difficult to directly associate this extended emission with the donor star. Fluorescent emission from the donor in this case

should manifest itself as a tightly concentrated spot situated on the positive V_y-axis.

In Fig. 11, we present a tomogram of the N III λ4640 emission line. The maximum entropy method of producing Doppler tomograms allows for a simultaneous fit to a number of different lines to produce one map. However, in this case the N III λ4640 line strongly dominates over any others in the Bowen blend. We see two regions of enhanced emission. The brighter of the two spots occurs at a combination of phasing and velocity where we would expect the donor star to be fluorescing. The small horizontal offset of $V_x \simeq 35 \pm 30\,\mathrm{km\,s^{-1}}$ is consistent with the errors in our ephemeris (±0.02 in phase).

The second spot occurs at a much lower velocity, and is 1σ–2σ weaker (relative to the local noise level) than the first. It is difficult to provide a truly satisfactory explanation for its origin. Perhaps, it traces some form of low-velocity outflow (e.g. disc wind), though why it should be preferentially observed at an apparent phase of ∼0.25 remains a mystery (orbital phase can be considered to increase in a clockwise fashion around a Doppler map).

If we presume that the bright spot in Fig. 11 is caused by the irradiated inner face of the donor star, this is an excellent tracer for the kinematics of the system. The precise location of the spot can be measured using a two-dimensional Gaussian fit (though bearing in mind that the actual shape of the spot is not expected to be Gaussian), providing a velocity of $K_{\mathrm{em}} = 245 \pm 30\,\mathrm{km\,s^{-1}}$. Using this value, we can shift all of our spectra into the rest frame of the (irradiated face of the) donor. A sharp N III λ4640 component is clearly resolved (Fig. 12). However, since this is a measure of the motion of the irradiated inner face of the donor star, it only provides us with a lower limit on the velocity of the centre of mass (see e.g. Steeghs & Casares 2002; Muñoz-Darias, Casares & Martinez-Pais 2005).

One final piece of information remains to be extracted from the Doppler tomograms; assigning the correct systemic velocity should produce the most sharply defined features in a Doppler map. We used the He II and N III Doppler maps to verify the systemic velocity. The χ^2 value of the map was calculated for a range of γ, and the best fit in terms of minimal χ^2 was achieved for $\gamma = 192 \pm 2\,\mathrm{km\,s^{-1}}$ for the N III map and $\gamma = 185 \pm 2\,\mathrm{km\,s^{-1}}$ for He II λ4686. These are both consistent with, if slightly higher than, the results derived from the He II λ4686 wings in Section 3.3. The complex, asymmetric core profile of the He II emission line could be contaminating one wing more than the other, leading to this small offset. We hereafter adopt the value for γ derived from the He II λ4686 Doppler map. This should be more reliable than the N III map since only a single, isolated emission line is involved in the fitting process, rather than the more complicated blend of Bowen lines.

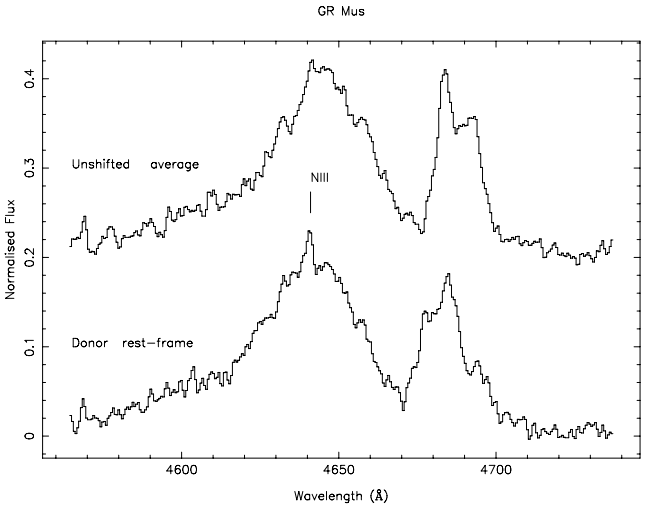

Figure 12. Average spectrum created by combining all of the individual unshifted spectra from our observations (top), showing the Bowen emission blend and He II λ4686 region. Below, this is shown the average spectrum when all of the individual spectra are shifted into the rest frame of the donor star. A sharp N III λ4640 component is clearly resolved.

4 DISCUSSION

4.1 Systemic velocity

Whilst the systemic velocities inferred from both the wings of the He II λ4686 line and the Doppler tomograms are self-consistent (∼185 $\mathrm{km\,s^{-1}}$), they are considerably higher than the earlier estimate by Cowley et al. (1988) ($98 \pm 10\,\mathrm{km\,s^{-1}}$). This measurement was obtained from rather low-quality data, with poor spectral and temporal resolution. Additionally, they based their measurements on the motion of the He II λ4686 line core. There are a number of different emitting regions which contribute to this line, leading to a complex core structure (see e.g. Figs 6 and 8). A basic measurement of the line centre under the assumption that this will accurately trace the motion of the compact object will therefore be subject to large systematic errors.

In light of this, we believe that our estimate for the systemic velocity will be a better reflection of the true value. Although large, our measurements do seem reasonable in the context of the high galactic latitude ($b = -6.42$) of GR Mus; the neutron star is likely to have received a substantial 'kick' out of the Galactic Plane at birth. A number of statistical studies on pulsar velocities have been carried out. These studies give a mean birth velocity of 100–500 $\mathrm{km\,s^{-1}}$, with some possessing velocities of $\geqslant$1000 $\mathrm{km\,s^{-1}}$ (Wang, Lai & Han 2006).

4.2 Interpretation of the Bowen blend Doppler map

The N III Doppler map (Fig. 11) appears to display enhanced emission in the region of and at the phasing where we would expect to see the companion star Roche lobe, in addition to an abundance of noisy structure in the outer regions of the map. A useful way to confirm the validity of the Doppler map is to observe the behaviour of sharp components in our trailed spectrogram (Fig. 5). This is not trivial due to the faintness of GR Mus compared to a system such as Sco X-1, which clearly features narrow Bowen lines moving in phase with the donor star (Steeghs & Casares 2002).

We can reconstruct an ideal trailed spectrogram from the Doppler tomograms to test for systematic residuals in the maps. As a test, we first apply this technique to the He II λ4686 emission line. The two distinct components we see in the Doppler map (Fig. 8) are reproduced clearly in the predicted trailed spectrogram (left-hand panel, Fig. 13) and can be easily identified in the observed data. For the case of the N III λ4640 emission line (Fig. 14), we again see two components in the reconstructed spectrogram, though not quite so distinctly as for the case of He II. Comparing this idealized image to the real data, it is indeed possible to detect faint traces of these two narrow, approximately antiphased lines which produce the two distinct spots in Fig. 11. The second spot is therefore unlikely to be a systematic residual produced when creating the Doppler map, and its unusual phasing/positioning could perhaps therefore be attributed to a region which violates one of the axioms of Doppler Tomography, for example that all motion should be parallel to the orbital plane.

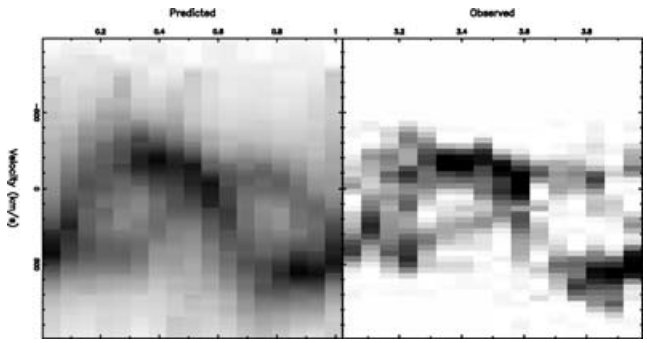

Figure 13. The right-hand panel displays the observed trailed spectra of the He II λ4686 emission line and the left-hand panel shows the ideal trailed spectrogram reconstructed from the Doppler tomogram shown in Fig. 8. Orbital phase is plotted along the *x*-axis.

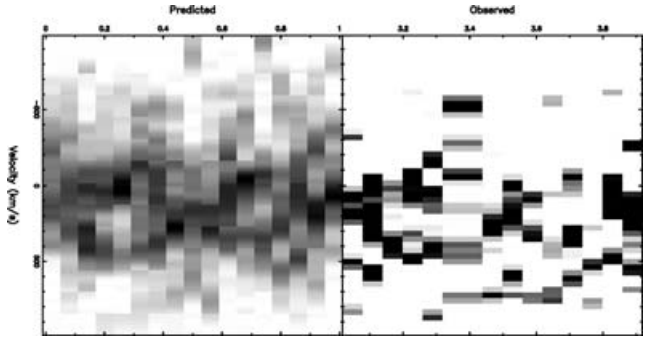

Figure 14. The right-hand panel displays the observed trailed spectra of the N III λ4640 emission line, part of the Bowen emission complex. Next to this is plotted the ideal trailed spectrogram reconstructed from the Doppler tomogram in Fig. 11. Orbital phase is plotted along the *x*-axis.

Note that a violation of these axioms does not mean that the map is erroneous, but it does complicate the successful interpretation of the map.

4.3 Refined mass limits

de Jong, van Paradijs & Augusteijn (1996) estimated an opening (semi-) angle for the accretion disc in GR Mus of $\sim 12^\circ$ using a simple geometric model for the reprocessing of X-rays in LMXBs. It is important to note that this value is hostage to the implicit assumptions underlying these models, for example the geometric description of the disc and of the X-ray emitter. This will entail a systematic uncertainty that likely exceeds the internal model accuracy of less than a degree. Nevertheless, this value agrees well with Motch et al. (1987) who estimated an opening angle of $\sim 9^\circ - 13^\circ$ in order to explain the observed amplitude of the orbital photometric modulation.

We can use this information to derive a mass estimate for the individual components by using the '*K*-correction' algorithm developed by Muñoz-Darias et al. (2005). This measures the deviation between the reprocessed light centre of the fluorescence emission lines and the centre of mass of a Roche lobe filling star in a persistent LMXB, including the screening effects by a flared accretion disc. Using the fourth-order polynomial fits given by Muñoz-Darias et al. (2005) for disc opening angles of 8°, 10°, 12° and 14° gives a total mass range for the neutron star of $1.20 \leqslant M_X/\mathrm{M}_\odot \leqslant 2.64$. Since the neutron star mass and the mass ratio are related by the mass function,[2] we obtain $0.32 \leqslant q \leqslant 0.43$, and limits on the companion mass of $0.45 \leqslant M_2/\mathrm{M}_\odot \leqslant 0.85$.

Table 2. Derived system parameters for GR Mus/XB 1254–690.

Parameter		Parameter	
$T_{\rm dip}$ (HJD)	245 3151.647 (3)	γ (km s^{-1})	185 ± 2
T_0 (HJD)	245 3151.509 (3)	q	0.32–0.43
K_1 (km s^{-1})	130 ± 16	$M_X(\mathrm{M}_\odot)$	1.20–2.64
$K_{\rm em}$ (km s^{-1})	245 ± 30	$M_2(\mathrm{M}_\odot)$	0.45–0.85

Note: Inclination constrained to 65°–73°.

This correction is dependent upon the opening angle of the accretion disc, monotonically decreasing with opening angle such that the largest opening angle gives the lowest neutron star mass. Since the largest opening angle we have used exceeds the estimates of both Motch et al. (1987) and Muñoz-Darias et al. (2005), this gives a very conservative lower limit to the neutron star mass, and the true value is unlikely to be so low. Equally, the upper limit is derived using an opening angle lower than that suggested by Motch et al. (1987) and as such the neutron star is unlikely to be quite so massive.

Limiting ourselves to a disc opening angle of exactly 12° (de Jong et al. 1996), the mass constraints upon the neutron star tighten up to $1.35 \leqslant M_X/\mathrm{M}_\odot \leqslant 2.32$, with $0.33 \leqslant q \leqslant 0.41$ and $0.49 \leqslant M_2/\mathrm{M}_\odot \leqslant 0.79$. These limits are not a vast improvement over the ones derived above using a range of opening angles from 8° to 14°. This indicates that the major source of uncertainty in this case is still incurred from the measurements of $K_{\rm em}$ and particularly of K_1 (see Section 3.3) in addition to the system inclination angle. The choice of disc opening angle (within a reasonable range) has only a small effect in comparison. Nevertheless, we feel it is prudent not to restrict our final mass estimate by the assumption of a disc opening angle of exactly 12°, preferring the more conservative range of 8°–14°. The derived parameters for GR Mus are listed in Table 2.

4.4 Roche lobe size

We know that the companion must be filling its Roche lobe in order to permit persistent accretion. There is a well known and useful relationship between the fractional Roche lobe radius and the mass ratio (Paczynski 1971) which can be combined with Kepler's third law to provide an estimate of the size of the Roche lobe as a function of period. In the case of this system (with a 3.9-h period), the relationship may be expressed as $R_L = 0.58 M_2^{1/3}$.

We can thus derive the range of potential Roche lobe radii consistent with the mass range of the companion star that we have derived kinematically. This turns out to be $0.44 \leqslant R_L/\mathrm{R}_\odot \leqslant 0.55$. Whilst at the lower end of our mass constraints the donor would be consistent with a main-sequence-like object as proposed by Motch et al. (1987), we cannot rule out the possibility that GR Mus harbours an overmassive evolved companion that has been stripped of its outer layers (e.g. King & Schenker 2002).

5 CONCLUSIONS

We have used the Bowen emission blend and Doppler tomography to trace for the first time the motion of the donor star in the persistent

[2] $f(M_X) = \dfrac{K_2^3 P_{\rm orb}}{2\pi G} = \dfrac{M_X \sin^3 i}{(1+q)^2}$.

LMXB GR Mus. This has allowed us to derive kinematical mass limits for this system. In combination with estimates for the opening angle of the accretion disc, and new measurements of the He II λ4686 emission line (in an attempt to trace the motion of the compact object), we have derived tentative new mass constraints of $1.20 \leqslant M_X/\mathrm{M}_\odot \leqslant 2.64$ for the compact object and $0.45 \leqslant M_2/\mathrm{M}_\odot \leqslant 0.85$ for the companion star.

We cannot rule out the possibility that GR Mus harbours an overmassive evolved companion star, or more intriguingly an overmassive neutron star. Tighter constraints on the system parameters may therefore have important implications for our knowledge of the equation of state of nuclear matter (e.g. Cook, Shapiro & Teukolsky 1994) or indeed on the formation scenarios for typical LMXBs (e.g. Pfahl, Rappaport & Podsiadlowski 2003).

Future investigations should also concentrate on determining the origin of the unusual second spot in the N III Doppler map (Fig. 11). This feature is hard to explain, and perhaps could be caused by a violation of the axioms of Doppler Tomography. Related to this point, the broad emission band seen in the left-hand side of the Doppler maps for He II and Hβ (in this system and a number of others) is of uncertain origin. We believe this emission to be produced in an extended disc bulge, but physical modelling will be necessary to confirm this.

ACKNOWLEDGMENTS

ADB was supported by a PPARC Research Studentship. DS acknowledges a Smithsonian Astrophysical Observatory Clay Fellowship as well as support through NASA GO grant NNG06GC05G. Based on observations made with ESO Telescopes at the Paranal Observatory under programme ID 073.D-0819. We gratefully acknowledge the use of the MOLLY and DOPPLER packages developed by T. R. Marsh.

REFERENCES

Augusteijn T., van der Hooft F., de Jong J. A., van Kerkwijk M. H., van Paradijs J., 1998, A&A, 332, 561
Buxton M., Vennes S., 2003, MNRAS, 342, 105
Casares J., Marsh T. R., Charles P. A., Martin A. C., Martin E. L., Harlaftis E. T., Pavlenko E. P., Wagner R. M., 1995, MNRAS, 274, 565
Casares J., Steeghs D., Hynes R. I., Charles P. A., O'Brien K., 2003, ApJ, 590, 1041
Casares J., Cornelisse R., Steeghs D., Charles P. A., Hynes R. I., O'Brien K., Strohmayer T. E., 2006, MNRAS, 373, 1235
Cook G. B., Shapiro S. L., Teukolsky S. A., 1994, ApJ, 424, 823
Cornelisse R., Steeghs D., Casares J., Charles P. A., Barnes A. D., Hynes R. I., O'Brien K., 2007, MNRAS, in press (doi:10.1111/j.1365-2966.2007.12193.x) (arXiv/0707.0449)
Courvoisier T. J. L., Parmar A. N., Peacock A., Pakull M., 1986, ApJ, 309, 265
Cowley A. P., Hutchings J. B., Crampton D., 1988, ApJ, 333, 906
de Jong J., van Paradijs J., Augusteijn T., 1996, A&A, 314, 484
Griffiths R. E., Gursky H., Schwartz D. A., Schwartz J., Bradt H., Doxsey R. E., Charles P. A., Thorstensen J. R., 1978, Nat, 276, 247
Hellier C., 2000, New Astron. Rev., 44, 131
Horne K., 1986, PASP, 98, 609
Hynes R. I., Charles P. A., Haswell C. A., Casares J., Zurita C., Serra-Ricart M., 2001, MNRAS, 324, 180
Hynes R. I., Charles P. A., van Zyl L., Barnes A., Steeghs D., O'Brien K., Casares J., 2004, MNRAS, 348, 100
Iaria R., DiSalvo T., Burderi L., Rossa N. R., 2001, ApJ, 548, 883
in't Zand J. J. M., Kuulkers E., Verbunt F., Heise J., Cornelisse R., 2003, A&A, 411, L487
Jahoda K., Swank J. H., Stark M. J., Giles A. B., Strohmayer T., Zhang W., Margan E. H., 1996, SPIE, 2808, 59
King A. R., Schenker K., 2002, in Gnsicke B. T., Beuermann K., Reinsch K., eds, ASP Conf. Ser. Vol. 261. The Physics of Cataclysmic Variables and Related Objects. Astron. Soc. Pac., San Francisco, p. 233
Levine A. M., Corbet R., 2006, ATel, 940, 1
Mason K. O., Middleditch J., Nelson J. E., White N. E., 1980, Nat, 287, 516
Marsh T. R., Horne K., 1988, MNRAS, 235, 269
Motch C., Pedersen H., Beuermann K., Pakull M. W., Courvoisier T. J. L., 1987, ApJ, 313, 792
Muñoz-Darias T., Casares J., Martinez-Pais I. G., 2005, ApJ, 635, 502
Paczynski B., 1971, ARA&A, 9, 183
Pearson K. J. et al., 2006, ApJ, 648, 1169
Pfahl E., Rappaport S., Podsiadlowski Ph., 2003, ApJ, 597, 1036
Schachter J., Filippenko A. V., Kahn S. M., 1989, ApJ, 340, 1049
Schneider D. P., Young P., 1980, ApJ, 238, 946
Smale A. P., Wachter S., 1999, ApJ, 527, 341
Smale A. P., Church M. J., Balucinska-Church M., 2002, ApJ, 581, 1286
Smith D. A., Dhillon V. S., 1998, MNRAS, 301, 767
Steeghs D., Casares J., 2002, ApJ, 568, 273
Uno S., Mitsuda K., Aoki T., Makino F., 1997, PASJ, 49, 353
van Paradijs J., McClintock J. E., 1995, in Lewin W. H. G., van Paradijs J., van der Heuvel P. J., eds, Optical and Ultraviolet Properties of X-ray Binaries. Cambridge Univ. Press, Cambridge
Wade R. A., Horne K., 1988, ApJ, 324, 411
Wang C., Lai D., Han J. L., 2006, ApJ, 639, 1007
Warner B., 1976, in Eggleton P., Mitton S., Whelan J., eds, IAU Symp. 73, Structure and Evolution of Close Binary Systems. Reidel, Dordrecht, p. 85

This paper has been typeset from a TEX/LATEX file prepared by the author.